Balancing Electronic Spin State via Atomically-Dispersed Heteronuclear Fe-Co Pairs for High-Performance Sodium-Sulfur Batteries

Canhuang Li, Jing Yu, Dawei Yang*, Hao Li, Yapeng Cheng, Yuchuan Ren, Xiaoyu Bi, Jiachen Ma, Ruirui Zhao, Yingtang Zhou*, Jian Wang, Chen Huang, Junshan Li, Ivan Pinto-Huguet, Jordi Arbiol, Haining Zhang*, Sen Xin*, Andreu Cabot*

C. H. Li, Dr. D. W. Yang
Henan Key Laboratory of Quantum Materials and Quantum Energy, School of Quantum Information Future Technology, Henan University, Kaifeng 475004, China
E-mail: dwyang@henu.edu.cn

C. H. Li, J. Yu, Dr. D. W. Yang, H. Li, Y. P. Cheng, Y. C. Ren, X. Y. Bi, C. Huang, Prof. A. Cabot
Catalonia Institute for Energy Research-IREC
Sant Adrià de Besòs, Barcelona 08930, Spain
E-mail: acabot@irec.cat

C. H. Li, C. Huang
Department of Chemistry, Universitat de Barcelona, Barcelona, 08028 Spain

H. Li, Y. P. Cheng
Wuhan University of Technology, Nr. 122 Luoshi Rd, Wuhan 430070, China.

J. Yu, I. Pinto-Huguet, Prof. J. Arbiol
Catalan Institute of Nanoscience and Nanotechnology (ICN2), CSIC and BIST, Campus UAB, Bellaterra, 08193 Barcelona, Catalonia, Spain

J. C. Ma
Research Center for Materials, Architectures and Integration of Nanomembranes (MAIN) Chemnitz University of Technology 09126 Chemnitz, Germany

Dr. R. R. Zhao
School of Chemistry, South China Normal University, Guangzhou 510006, P. R. China

Dr. J. Wang
Helmholtz Institute Ulm (HIU), D89081 Ulm, Germany

Dr. J. S. Li
Institute for Advanced Study, Chengdu University, 610106, Chengdu, P. R. China

Prof. Y. T. Zhou
National Engineering Research Center for Marine Aquaculture, Marine Science and Technology College, Zhejiang Ocean University, Zhoushan, Zhejiang Province, 316004 China
E-mail: zhouyingtang@zjou.edu.cn

Prof. H. N. Zhang
State Key Laboratory of Advanced Technology for Materials Synthesis and Processing, Wuhan University of Technology, Nr. 122 Luoshi Rd, Wuhan 430070, China.
E-mail: haining.zhang@whut.edu.cn

Prof. S. Xin
CAS Key Laboratory of Molecular Nanostructure and Nanotechnology, CAS Research/Education Center for Excellence in Molecular Sciences, Beijing National Laboratory for Molecular Sciences, Institute of Chemistry, Chinese Academy of Sciences (CAS), Beijing 100190, China.
E-mail: xinsen08@iccas.ac.cn

Prof. J. Arbiol, Prof. A. Cabot
ICREA Pg. Lluis Companys, 08010 Barcelona, Catalonia, Spain

ABSTRACT

Room-temperature sodium-sulfur (Na-S) batteries are emerging as a promising next-generation energy storage technology, offering high energy densities at low cost and utilizing abundant elements. However, their practical application is hindered by the shuttle effect of sodium-polysulfides and the sluggish kinetics of sulfur redox reactions. In this study, we demonstrate a heteronuclear diatomic catalyst featuring Fe and Co bimetallic sites embedded in nitrogen-doped hollow carbon nanospheres (Fe-Co/NC) as an effective sulfur host at the cathode of Na-S batteries. Aberration-corrected high-angle annular dark field scanning transmission electron microscopy demonstrates the presence of isolated Fe-Co atomic pairs, while synchrotron radiation X-ray absorption fine structure analysis confirms the ($Fe\text{-}Co\text{-}N_6$) coordination structure. Density functional theory calculations show that the introduction of Fe atoms induces electron delocalization in Co(II), shifting the electronic configuration from a low-spin to a higher-spin state. This shift enhances the hybridization of the Co dz^2 orbitals with the antibonding π orbitals of sulfur atoms within the sodium sulfide species that accelerates their catalytic conversion. As a result, Fe-Co/NC-based cathodes exhibit excellent cycling stability (378 mAh g^{-1} after 2000 cycles) and impressive rate performance (341.1 mAh g^{-1} under 5 A g^{-1}).

1. Introduction

Room-temperature sodium-sulfur batteries (SSBs) have attracted significant attention as promising next-generation energy storage systems.[1-3] However, their practical application is hindered by the sluggish kinetics of the redox reactions between S_8 and Na_2S.[4-7] To address this issue, first-row transition metal catalysts, such as Mn, Fe, Co, and Ni, are often incorporated into carbon-based cathode hosts. The 3d unoccupied orbitals of the transition metals interact with polysulfides, weakening their bonding strength and promoting the reduction of sulfur.[8-13] Despite these advantages, the high molar mass of metals often lowers the theoretical capacity of the resultant cathodes, making the products less competitive in high-capacity demands.[14-15]

To minimize the catalyst weight, single-atom catalysts (SACs) provide a promising solution for SSBs due to their superior catalytic performance and maximized metal utilization efficiency.[16-19] Extending this concept, diatomic catalysts (DACs) introduce a bimetallic coordination environment, offering additional flexibility to modify the electronic structure and shift the metal d-band center at the atomic level.[20-23] However, the performance of SACs and DACs is highly dependent on the coordination environment, which control and investigation remain challenging.

In this work, we first report the synthesis of a DAC composed of Fe-Co dual sites anchored on hollow N-doped carbon spheres (Fe-Co/NC) in Na-S batteries. We use aberration-corrected high-angle annular dark field scanning transmission electron microscopy (AC HAADF-STEM) and synchrotron radiation X-ray absorption spectroscopy (XAS) to investigate the Fe-Co atomic pairs and their coordination structure. Furthermore, density functional theory (DFT) calculations are employed to examine the influence of Fe atoms on electron delocalization and the spin state of Co(II). The combined experimental and theoretical findings are then correlated with the adsorption and catalytic performance of the materials, as well as the performance of the cells incorporating these catalytic additives.

2. Results and Discussion

DFT results indicate that the presence of Fe atoms within the Fe-Co/NC structure reduces the energy gap between the Co dxy and dz2 orbitals, owing to the coupling between Co 3d and Fe 3d orbitals. This reduction facilitates the transition of electrons to the eg orbital (Figure 1a).

Simultaneously, the limited number of eg electrons and the small occupancy of the Co(II) dz2 orbital cause the Co d band to shift upward (Figure 1b). As a result, the antibonding orbital moves closer to the Fermi level, reducing the number of antibonding electrons.[5, 24] This shift strengthens the interaction between Co atoms in Fe-Co/NC and Na-S reaction intermediates, enhancing NaPS adsorption by forming a σ* orbital bond with sulfur (Figure 1c).

Additionally, the introduction of Fe alters the electron configuration of the Co/NC matrix from a low-spin (LS) to a high-spin (HS) state, thereby increasing the unpaired electrons of Co/NC from 0.35 e/Å^3 to 0.47 e/Å^3 in Fe-Co/NC (Figures 1d-e). This shift raises the effective magnetic moment from 1.52 μB in Co/NC to 1.87 μB in Fe-Co/NC (Figure 1f). The Fe-Co/NC material also exhibits a higher density of states near the Fermi level compared to Co/NC (Figure 1g), suggesting that the Fe incorporation enhances the material's conductivity, potentially accelerating reaction kinetics. The spin density isosurface confirms that Fe-Co/NC contains more unpaired electrons, which can form covalent bonds with sulfur, improving the anchoring of sodium polysulfides (NaPSs) and enabling more efficient sulfur conversion (**Figure 1h**).

Overall, DFT calculations suggest that the introduction of Fe atoms into the Co/NC microenvironment successfully manipulates the electronic spin and energy of the 3d Co electrons, which is expected to have a significant impact on the catalytic activity towards the sulfur redox reaction in SSBs.

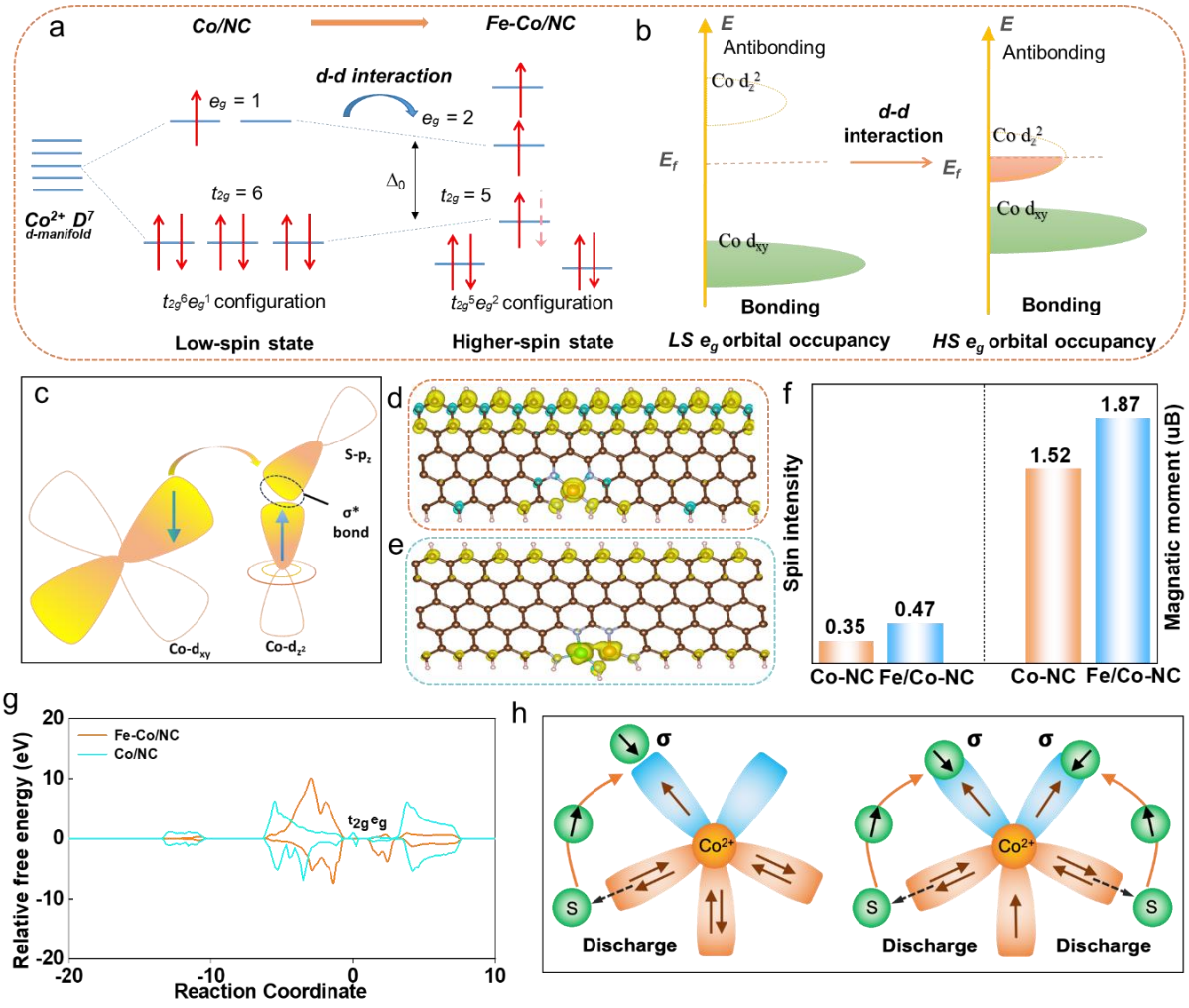

Figure 1. (a) Energy level diagram of the interaction between Co/NC and Fe-Co/NC monolayer molecular orbitals at different energy levels. (b) Energy level transition diagram between Co/NC and Fe-Co/NC. (c) Schematic diagram of the interaction between the d orbital of Co and the p orbital of S. (d,e) Spin density of Co/NC (d) and Fe-Co/NC (e). Brown balls represent carbon atoms, grey balls represent nitrogen atoms, orange balls represent cobalt atoms and green balls represent iron atoms). (f) Spin density and spin moment of Co/NC and Fe-Co/NC. (g) Density of states of Co/NC and Fe-Co/NC. (h) Schematic diagram of sulfur transformation regulated by spintronics in Co/NC (left) and Fe-Co/NC (right).

The process used to produce Fe-Co/NC is illustrated in **Figure 2a**.[25-26] It begins with a two-step solvent impregnation method. First, Co is introduced to the surface of polydopamine-coated silica nanospheres (SiO_2-PDA), followed by the addition of a ferric nitrate solution. Subsequent high-temperature annealing, along with the application of strong acid, removes the SiO_2

template and any excess unstable metal elements, resulting in $FeCoN_6$ supported by nitrogen-doped hollow carbon spheres (Fe-Co/NC). Co/NC and Fe/NC reference samples were produced in the same way, but using just one of the metal precursors. The Brunauer-Emmett-Teller (BET) specific surface area of Fe-Co/NC, Fe/NC and Co/NC was estimated at 659 $cm^2 g^{-1}$, 621 $cm^2 g^{-1}$ and 639 $cm^2 g^{-1}$ (Figure S1). These large values facilitate the effective dispersion of the catalyst, as well as S and Na_2S. However, their similar magnitudes will not influence the comparative analysis of the samples.

Similar X-ray diffraction (XRD) patterns were measured from Fe-Co/NC, Co/NC, and Fe/NC, with characteristic peaks at 26° and 44° (Figures S2), corresponding to the (002) and (100) planes of graphitized carbon. Notably, no diffraction peaks associated with metal-based compounds were detected.[27]

Scanning electron microscopy (SEM) analysis reveals Fe-Co/NC consists of relatively uniformly sized spherical particles (Figure S3). Transmission electron microscopy (TEM) images further confirm that the Fe-Co/NC spheres are hollow, with a diameter of approximately 250 nm (**Figure 2b**).

A large number of paired metal atoms are observed in the AC HAADF-STEM image in **Figure 2c**, highlighted by red circles. The HAADF-STEM intensity shown in Figure 2e is directly related to the square of the atomic number of the imaged atom. The plotted profiles clearly show that, in each atomic pair, one atom consistently exhibits slightly higher intensity than the other. This suggests that one atom corresponds to Fe, while its paired counterpart corresponds to Co. Upon further magnification, it is observed that the distance between the adjacent Fe and Co atoms is approximately 2.4 Å **(Figures 2d,e** and S4). This distance is consistent with the effective diameter of Fe–Co interaction, further evidencing the construction of Fe-Co dimer structures.[25-26] STEM-EDX elemental mapping images confirm the uniform distribution of C, N, Co, and Fe in Fe-Co/NC **(Figure 2f)** . The Fe/NC and Co/NC materials also exhibit a similar hollow carbon sphere morphology with a uniform distribution of metal atoms, as shown in Figures S5 and S6. Inductively coupled plasma-atomic emission spectrometry (ICP-AES) analysis of Fe-Co/NC revealed a Fe content of 1.35% and a Co content of 1.52%. TEM-EDX analyses in Figures S7-9 show that the nitrogen content in Fe-Co/NC, Co/NC and Fe/NC is 3.4%, 2.34%, and 1.38%, respectively.

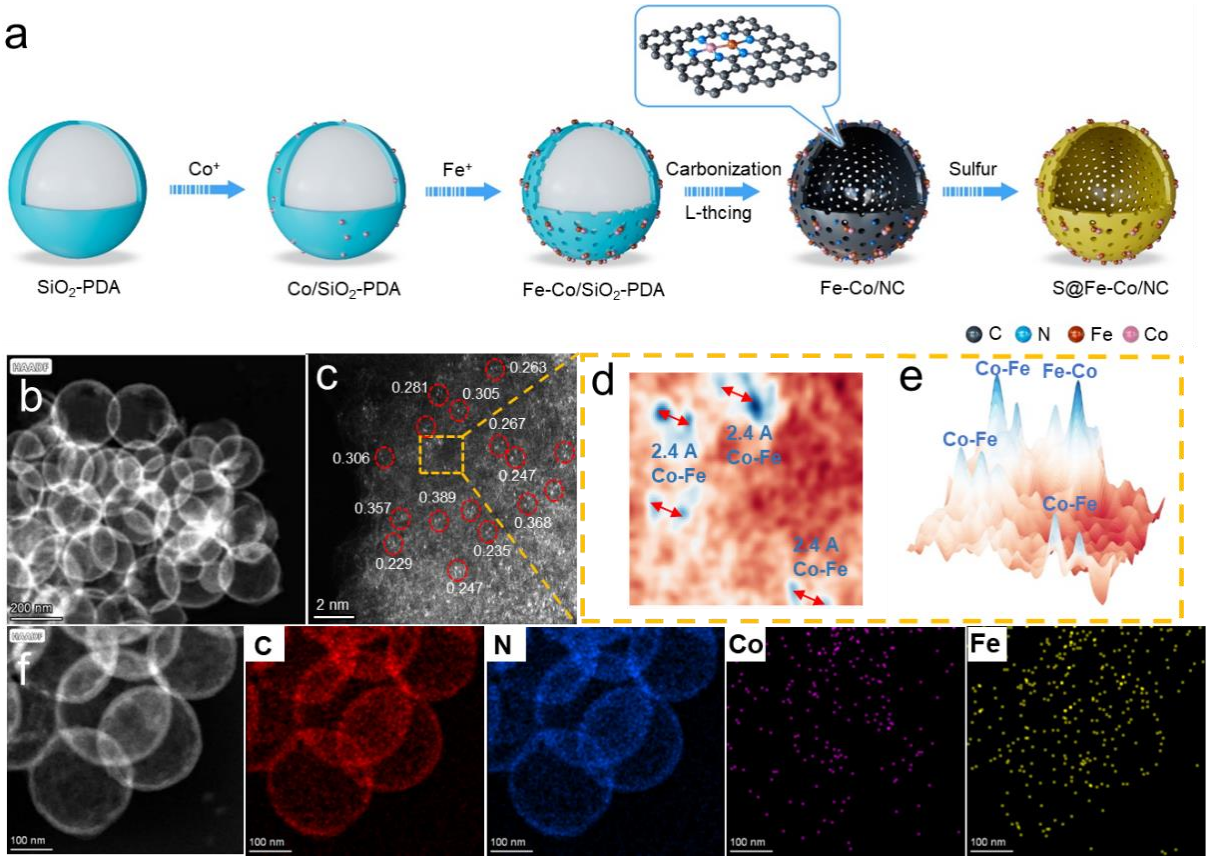

Figure 2. (a) Schematic illustration of the synthesis of Fe-Co/NC and S@Fe-Co/NC.[25-26] (b) TEM images of Fe-Co/NC. (c) AC HAADF-STEM image of Fe-Co/NC. Red circles display Fe-Co diatomic sites shown as bright contrast double spots. (d) Two-dimensional and (e) three-dimensional intensity profiles from the yellow-squared area in (c). (f) HAADF-STEM image and corresponding STEM-EDX mapping showing the elemental distribution of Fe-Co/NC.

The high-resolution N 1 s X-ray photoelectron spectroscopy (XPS) spectrum of the SACs and DACs (Figure S10) reveals five distinct peaks at 395.8 eV, 396.9 eV, 398.1 eV, 399.3 eV and 401.9 eV attributed to pyridine nitrogen, Fe(Co)-N bonds, pyrrolic nitrogen, graphitized nitrogen and oxide nitrogen, respectively.

To investigate the atomic structural and coordination environment of Fe-Co/NC in more detail, the Fe and Co K-edge of the samples were analyzed using X-ray absorption near-edge structure (XANES) and X-ray absorption fine structure (EXAFS) spectroscopies.[28-29] The Co K-edge XANES spectrum, displayed in **Figure 3a**, was compared to cobalt phthalocyanine (CoPc), cobalt metal foil (Co-foil), cobalt(II) oxide (CoO), and cobalt(III) oxide (Co_2O_3). The XANES results showed that the Co K-edge for Fe-Co/NC lies between those of Co-foil and CoO,

suggesting that the oxidation state of cobalt in Fe-Co/NC falls between 0 and +2, indicating partial oxidation. Similarly, the Fe K-edge XANES spectrum of Fe-Co/NC **(Figure 3b)** places the oxidation state of iron in Fe-Co/NC between that of metallic Fe (Fe-foil) and iron(III) oxide (Fe_2O_3), close to that of iron(II) oxide, suggesting that there is localized charge transfer at the metal sites.

In the Co K-edge Fourier-transformed EXAFS spectrum (Figure 3c and Table S1), two distinct peaks are observed: one at 1.4 Å, which corresponds to Co-N coordination, and another at 2.4 Å, attributed to Co-Fe coordination. The coordination numbers associated with these peaks are 3.1 and 0.8, respectively. Similarly, the Fe K-edge EXAFS spectrum (Figure 3d and Table S2) reveals peaks at comparable positions, with a 1.4 Å peak corresponding to Fe-N coordination and a 2.6 Å peak indicating Fe-Co coordination. The coordination numbers in this case are also very similar, measured at 3.2 and 0.8, respectively. Notably, the absence of any Co-Co and/or Fe-Fe coordination peak confirms that cobalt and iron are atomically dispersed within the material.

As shown in **Figure 3e,f,** the K-edge EXAFS fitting curves displayed that the experimental results were consistent with theoretical results when employing Co-N, Fe-N, and Fe-Co scattering paths. The EXAFS wavelet transform (WT) analysis with high resolution in both R- and k-spaces was used to further visualize the coordination configuration (**Figure 3g,h**). The WT contour plots of both Co and Fe for Fe-Co/NC exhibit two characteristic centers that are similar to the cobalt phthalocyanine (CoPc) and iron phthalocyanine (FePc), this further confirms the nitrogen coordination environment of the metal atom (Figures S13 and S14).

Overall, the above analysis results demonstrate that the Fe and Co atoms are coordinated with nitrogen within a Fe/Co-N_6 coordination structure and with each other, and confirm their atomic-level dispersion in the Fe-Co/NC structure.

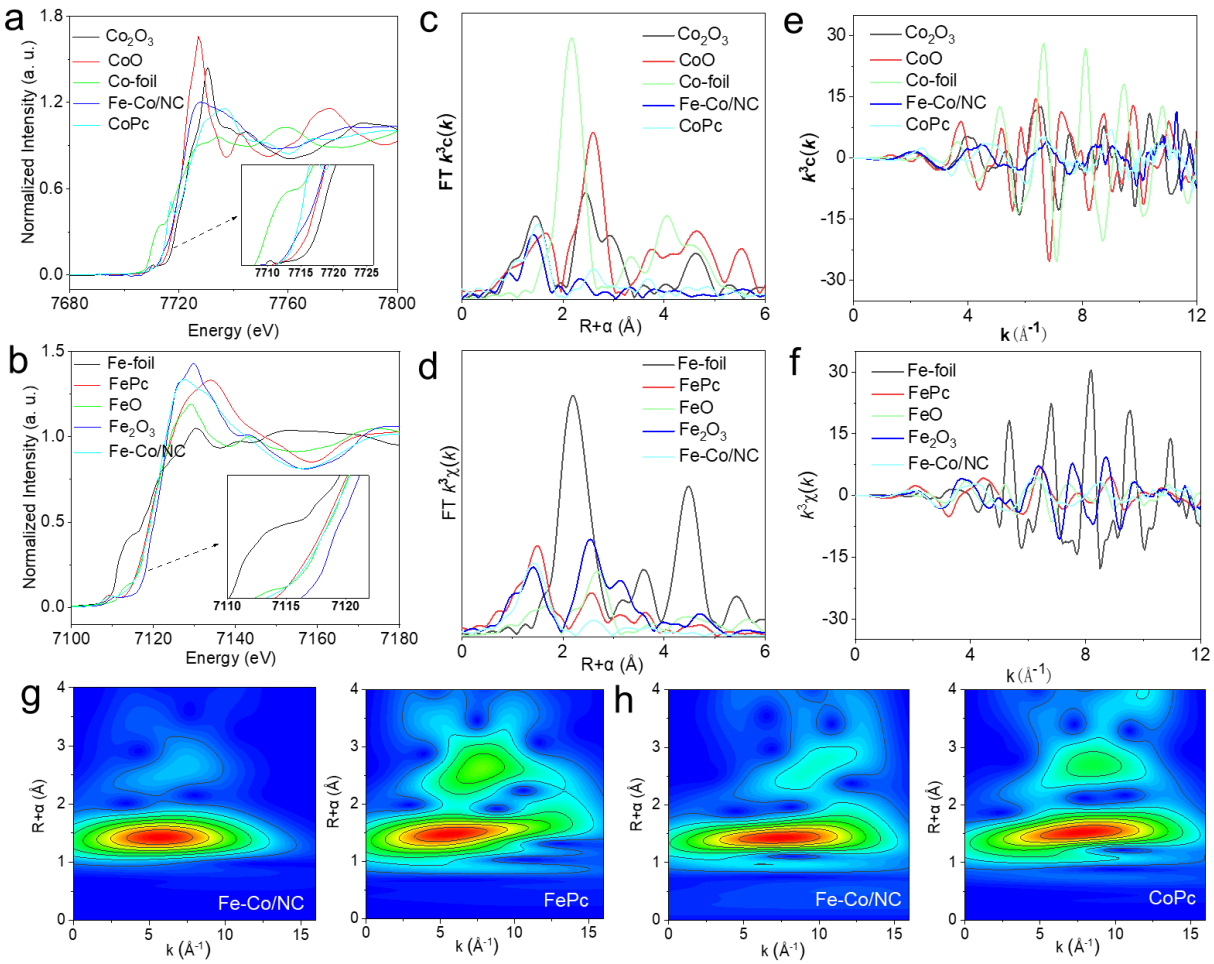

Figure 3. (a) Co K-edge XANES spectra, (b) Fe K-edge XANES spectra, (c) k^3-weighted χ(k)-function of Co-EXAFS spectra, (d) k^3-weighted χ(k)-function of the Fe-EXAFS spectra of Fe-Co/NC, FePc, Fe foil, FeO and Fe_2O_3, (e) EXAFS oscillations of Fe-Co/NC, CoPc, Co foil, CoO and Co_2O_3. (f) EXAFS oscillations of Fe-Co/NC with respect to the reference samples. (g) Fe k-edge WT-EXAFS spectra of Fe-Co/NC and FePc. (h) Co k-edge WT-EXAFS spectra of Fe-Co/NC and CoPc .

To evaluate the electrochemical performance of Fe-Co/NC as a sulfur host in SSBs, sulfur was incorporated into the Fe-Co/NC framework by a melt-infiltration process. XRD patterns and thermogravimetric analysis data confirmed that approximately 50% of sulfur was successfully integrated into the Fe-Co/CN host (Figures S2 and S15). The S redox behavior within Fe-Co/NC/S and the reference Fe/NC/S and Co/NC/S electrodes were explored in coin-type cells using a sodium metal anode and a 1.0 M $NaClO_4$ electrolyte using cyclic voltammetry (CV) at a scan rate of 0.1 mV s^{-1}. As shown in **Figure 4a**, all three electrodes exhibited two cathodic

peaks at the discharge process, attributed to the stepwise conversion of S_8 to Na_2S. A single anodic peak in the charging process is attributed to the gradual Na_2S reaction to S_8. For the Fe-Co/NC/S electrode, the voltage between the second cathodic and anodic peaks was 0.87 V, clearly below the 0.92 V and 1.04 V polarization obtained from Co/NC and Fe/NC electrodes, respectively.[24, 30] Even at high scan rates, the shape of the curve was preserved, indicating notable cycling stability (Figure S16). Fe-Co/NC/S provided the highest redox peak currents, pointing to a superior catalytic ability to promote NaPSs conversion to Na_2S. CV tests at different scan rates were used to calculate the Na^+-ion diffusivity on the various host materials in Figure S17. For Fe-Co/NC, the diffusivity was determined to be $2.2 \cdot 10^{-7}$ cm^2 S^{-1} and $3.3 \cdot 10^{-7}$ cm^2 S^{-1}, significantly outperforming Co/NC ($1.04 \cdot 10^{-7}$ cm^2 S^{-1}, $1.3 \cdot 10^{-7}$ cm^2 S^{-1}) and Fe/NC ($1.5 \cdot 10^{-7}$ cm^2 S^{-1}, $1.4 \cdot 10^{-7}$ cm^2 S^{-1}).

The rate performances of the different cells are shown in **Figure 4b**. Fe-Co/NC/S exhibited the best rate performance, with an initial capacity of 1353 mAh g^{-1} at 0.1 A g^{-1}, and reversible capacities of 971, 810, 683, 628, 490, 337 mAh g^{-1} at 0.3, 0.5, 1, 2, 3 and 5 A g^{-1}, respectively. The corresponding charging and discharging profiles obtained at different current densities are shown in Figure S18. Fe-Co/NC/S maintains the charging and two discharging plateaus even at a high current density of 5 A g^{-1}, consistent with a high catalytic activity. It is worth mentioning that under the same measurement conditions, the capacity obtained by the pure Fe-Co/NC electrode without sulfur was negligible (Figure S19).

The long-term cycle stability of Fe-Co/NC/S and the two reference electrodes is shown in **Figure 4d**. Fe-Co/NC/S showed an initial capacity of 593 mAh g^{-1} at 1 A g^{-1}, while the initial capacities of Co/NC and Fe/NC are 539 and 323 mAh g^{-1}. After 2000 cycles, Fe-Co/NC retained 379 mAh g^{-1}, which represents a 0.018% capacity loss per cycle, while the Co/NC and Fe/NC failed after 1300 and 500 cycles, respectively. Even at a high current density of 3 A g^{-1}, the Fe-Co/NC/S cathode retained a capacity of 370 mAh g^{-1} after 500 cycles **(Figure 4e)** . We further tested the cathode performance under a high sulfur loading, which is an essential parameter for practical applications. At a sulfur loading of 3.2 mg cm^{-2}, the Fe-Co/NC cathode exhibited an outstanding initial capacity of 1543 mAh g^{-1}, i.e. 4.94 mAh cm^{-2}, at 0.1 A g^{-1}, retaining 2.24 mAh cm^{-2} after 70 cycles **(Figure S20**. Besides, at a sulfur loading of 5.6 mg cm^{-2}, the Fe-Co/NC cathode exhibited an initial capacity of 1361 mAh g^{-1}, i.e. 4.36 mAh cm^{-}

^{2}, at 0.1 A g^{-1}, retaining 1.57 mAh cm^{-2} after 100 cycles **(Figure 4c)** . The initial low Coulombic efficiency, particularly noticeable at high sulfur loading, is attributed to the reaction between sulfur and the carbonate electrolyte.

Fe-Co/NC-based cells were evaluated over a wider temperature range to assess their potential for practical applications. Figure S21 presents the specific capacity over 100 cycles for cells tested at 0°C and 60°C. At 60°C, the battery's initial capacity was 568 mAh g^{-1}, decreasing to 300 mAh g^{-1} after 100 cycles. Likewise, at 0°C, the initial capacity started at 442 mAh g^{-1} and dropped to 243 mAh g^{-1} over the same cycle count. At 0°C, the initial battery capacity was 568 mAh g^{-1}, which decreased to 300 mAh g^{-1} after 100 cycles. Similarly, at 60°C, the initial capacity was 442 mAh g^{-1}, retaining 243 mAh g^{-1} after 100 cycles. These results demonstrate the robustness and feasibility of Fe-Co/NC-based cells under extreme climatic conditions.

After 200 cycles at 1 A g^{-1}, coin cells were disassembled, and their components were analyzed. The cathode material retained its original architecture, highlighting the effectiveness of the hollow structure in accommodating the volume expansion of sulfur during cycling (Figure S22). The Na anode of the Fe-Co/NC-based cell showed an even surface with a minimal amount of sulfur, according to SEM-EDS analysis **(Figures 4f** and S23a**)** . Besides, optical images show the separator to be almost transparent. In contrast, the anodes of Co/NC- and Fe/NC-based cells show a relatively uneven surface with a notable amount of S, compared with the anode of the Fe-Co/NC-based cell. Besides, their separator became colored owing to the presence of polysulfides.

Overall, these results highlight the crucial role of both Fe and Co in trapping polysulfides and facilitating the conversion of S_8 to Na_2S, thereby enhancing electrochemical stability. Additionally, a summary of the advancements achieved in this work compared to previously reported studies is provided in Table S3.

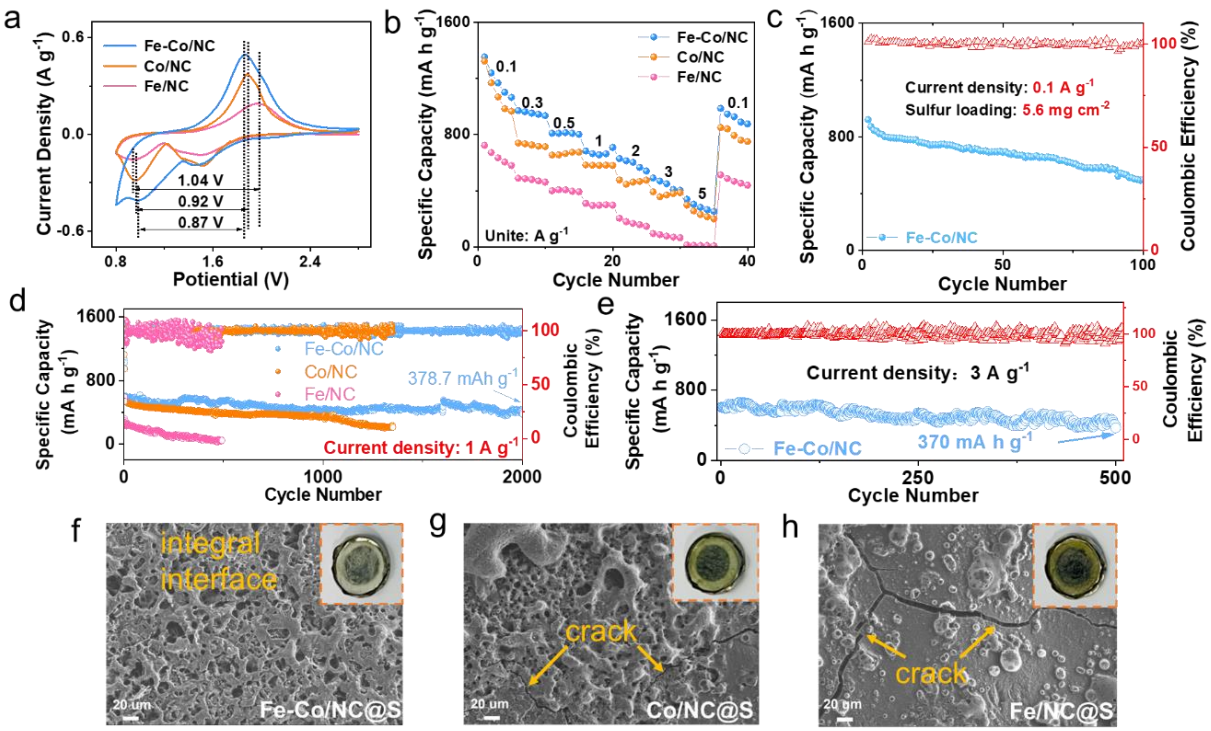

Figure 4. Electrochemical performance of SSBs with different cathodes. (a) CV profiles. (b) Rate capabilities. (c) Cycling performances at 0.1 A g^{-1} of an SSB based on a Fe-Co/NC/S cathode containing 5.6 mg cm^{-2} of S. (d) Long-term cycling at 1 A g^{-1}. (e) Cycling stability of the Fe-Co/NC-based SSB at 3 A g^{-1}. (f-h) SEM images of the surface of the sodium anodes disassembled from cycled coin cells (200 cycles) after cycling. Inset images show the separators.

To gain insight into the origin of the excellent performance of the Fe-Co/NC host, Na_2S_6 adsorption experiments were performed. **Figure 5a** displays optical images of vials containing equal amounts of Fe-Co/NC, Co/NC and Fe/NC within a Na_2S_6 solution after overnight adsorption. The Na_2S_6 solutions containing Fe-Co/NC and especially Fe/NC exhibit a significantly lighter colour than the solution containing Co/NC, indicating a stronger ability to adsorb polysulfides by the former materials. The supernatants were further analyzed by UV-vis spectroscopy. UV-vis spectra show that the obvious absorption band of Na_2S_6 in the range of 400-430 nm slightly faded in the presence of Co/NC, while notably decreased in the presence of Fe-Co/NC and especially Fe/NC **(Figure 5b)** .

High-resolution XPS analysis (Figure S24) was performed to examine changes in the valence states of N, Fe, and Co elements in Fe-Co/NC after Na_2S_6 adsorption. The N 1s spectrum showed a shift to lower binding energies, indicating a decrease in the electronegativity of the

chemical environment due to interactions between nitrogen atoms and sodium ions. Conversely, the high-resolution Co 2p and Fe 2p XPS spectra shifted to higher binding energies. This shift suggests an increase in the electronegativity of the chemical environment, attributed to the interaction between Fe and Co atoms and the sulfur atoms in NaPS.

DFT calculations were further employed to assess the interactions between NaPSs and the various host materials. The optimized adsorption configurations of NaPS species on different materials are shown in Figures S25-S27. As illustrated in **Figure 5c,d**, Fe-Co/NC demonstrated intermediate binding energies (Eb) for different NaPS species compared to the higher Eb observed for Fe/NC and the lower Eb for Co/NC. These DFT results align well with the experimental adsorption data presented earlier. The relatively low polysulfide adsorption capacity of Co/NC corresponds to its moderate catalytic activity in polysulfide conversion. Conversely, while Fe/NC shows a higher adsorption capacity for NaPSs, its catalytic activity is lower than that of Fe-Co/NC. This discrepancy is attributed to the strong binding energy of Fe/NC, which stabilizes the adsorption configuration, potentially inhibiting the polysulfide transformation. This finding supports the idea that overly strong or weak adsorption hinders the conversion process, a balance that Fe-Co/NC appears to achieve more effectively.[31-32]

The electrocatalytic activity of Fe-Co/NC on NaPSs conversion was further examined by CV in symmetric cells. As shown in **Figure 5e**, cells assembled with two identical electrodes, without sulfur, but with a Li_2S_4-based electrolyte, exhibited a pair of reversible redox peaks. Notably, the Fe-Co/NC-based cell demonstrated a higher current density and a lower onset potential for the redox peaks compared to cells with Fe/NC or Co/NC electrodes. This observation confirms the enhanced catalytic ability of Fe-Co/NC in promoting NaPS conversion.

Additionally, potentiostatic measurements at 1.3 V revealed that the Fe-Co/NC-based cell exhibited a higher current peak and a shorter nucleation time than the other cells (**Figure 5f**). By integrating the current-time curve, the nucleation capacity of Fe-Co/NC was calculated to be 241.1 mAh g^{-1}, significantly surpassing that of Co/NC (147.5 mAh g^{-1}) and Fe/NC (103.6 mAh g^{-1}). These results suggest that Fe-Co/NC not only accelerates NaPS conversion but also enhances Na_2S/Na_2S_2 deposition.

DFT calculations were used to evaluate the reaction kinetics of the charging process on Co/NC, Fe/NC and Fe-Co/NC surfaces (**Figures 5g** and S28-S30). The results revealed that the energy barrier for Na_2S decomposition on Fe-Co/NC is 0.89 eV, significantly lower than the barriers observed on Co/NC (1.34 eV) and Fe/NC (1.76 eV). This lower energy barrier is consistent with the enhanced redox transformation between Na_2S and NaPSs in Fe-Co/NC, further confirming its superior catalytic performance in facilitating the charging process of SSBs.

The free energy evolution profiles for the sulfur reduction reaction on Fe-Co/NC, shown in **Figure 5h**, demonstrate that the thermodynamic reduction process is more favorable on Fe-Co/NC compared to Co/NC and Fe/NC. This is particularly evident in the key transition from Na_2S_4 to solid Na_2S_2, where Fe-Co/NC exhibits a significantly lower energy barrier (0.65 eV) than Co/NC (0.70 eV) and Fe/NC (0.73 eV).

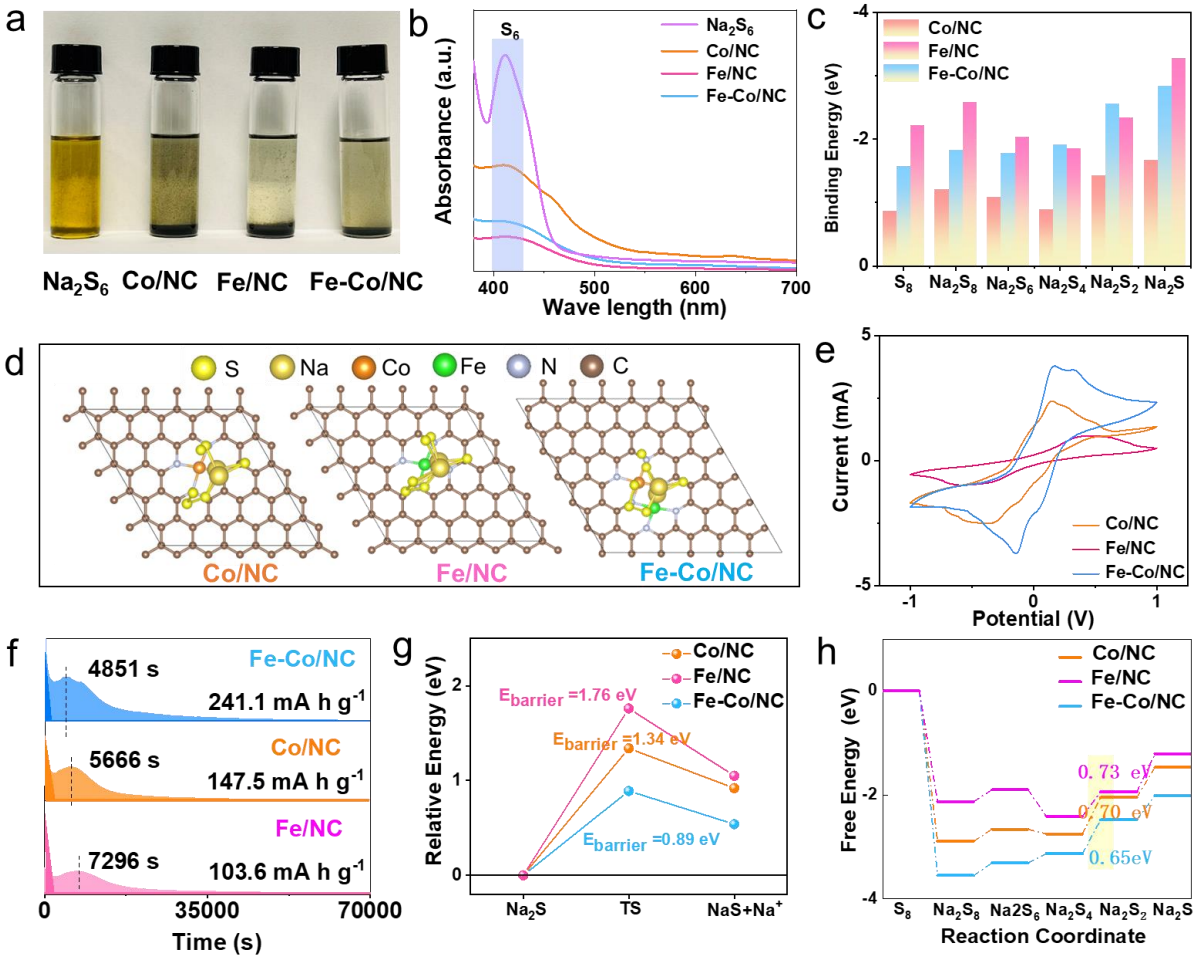

Figure 5. (a) Optical photograph of flasks containing a Na_2S_6 solution and the different adsorbents after one night of adsorption. (b) UV-vis spectrum of the polysulfide solutions. (c)

Binding energies of NaPSs on the surface of the different materials. (d) Adsorption model of Na_2S_6 on the different materials. (e) CV curves of Fe-Co/NC, Co/NC and Fe/NC symmetric cells. (f) Potentiostatic nucleation curves of Na_2S with Fe-Co/NC, Co/NC, and Fe/NC electrodes. (g) Na_2S decomposition energy barriers on different materials. (h) Gibbs free energy profiles of NaPSs species on the surface of Fe-Co/NC, Co/NC and Fe/NC.

Charging and discharging in SSBs is a complex electrochemical process, where resistance fluctuations indicate changes in charge transfer capabilities. Due to the limitations of CV in analyzing battery kinetics, we explored this process from a different perspective using electrochemical impedance spectroscopy (EIS) and distribution of relaxation times (DRT) analysis. First, EIS was employed to evaluate fully charged and discharged SSBs over a cycle (**Figure 6a**). The Fe-Co/NC-based battery displayed a lower charge transfer resistance (Rct) of 130.6 Ω, compared to Co/NC (145.7 Ω) and Fe/NC (210.5 Ω), indicating enhanced charge transfer efficiency. To further understand the overlapping relaxation processes, DRT analysis was applied, decomposing the EIS data into distinct local maxima, each representing a specific electrochemical process. The time constant (τ) corresponds to different polarization processes, while the peak area represents polarization resistance (Rp). As shown in **Figure 6b**, four peaks were identified in all batteries, corresponding to interphase contact resistance (P1), charge transfer resistance (P2), polysulfide diffusion resistance (P3), and ion diffusion resistance (P4).[31] The Fe-Co/NC-based battery exhibited the lowest impedance across all processes, particularly in interface and sodium ion diffusion impedance. This suggests that Fe-Co/NC enhances sodium ion transport and reduces NaPS accumulation at sulfur cathodes, confirming its superior catalytic activation on the S cathode.

To further study the transformation of amorphous sulfur, the Co-Fe/NC-based Na-S battery was subjected to *ex situ* XPS analysis during discharge to 1.5 V and 0.8 V, as well as charge to 1.5 V and 2.8 V **(Figure 6c)** .[33] In the initial stage, the S 2p XPS spectrum shows a doublet at 163.5 eV (S $2p_{3/2}$), assigned to S_8 molecules. A second doublet at around 168.0 eV (S $2p_{3/2}$) is associated with sulfate species generated by the surface oxidation of S. After discharging to 1.5 V, a new doublet appears at 161.5 eV (S $2p_{3/2}$) and it is attributed to Na_2S_2. Upon further discharging to 0.8 V, the intensity of the Na_2S_2 doublet is reduced and another lower energy

doublet appears at around 159.4 eV (S $2p_{3/2}$), which is associated with the conversion from Na_2S_2 to Na_2S. Additionally, a component associated with the oxidation of the NaPSs is detected at around 166.0 eV (S $2p_{3/2}$).

To further verify the reaction mechanism on Fe-Co/NC@S and Co/NC@S cathodes during the discharge/charge process, *in situ* Raman characterization was carried out, as displayed in **Figures 6d** and S31. The characteristic Raman peak of S_2^{2-} at about 426 cm^{-1} was the only signal observed in the initial discharge process.[34-35] According to the CV curve of Fe-Co/NC and Co/NC, the initial rapid potential drop represents the conversion of the long-chain Na_2S_x ($4 \leq x \leq 8$) to short-chain Na_2S_x ($1 < x \leq 3$). As the discharge progressed, the Raman signal of Na_2S_2 gradually diminished and eventually disappeared in the Fe-Co/NC@S cathode, indicating the complete conversion of Na_2S_2 to Na_2S. In contrast, the S_2^{2-} Raman peak was still detectable throughout the full discharge process on the Co/NC@S cathode.

The above results demonstrate that the presence of both Fe and Co in the Fe-Co/NC catalysts enables the complete transformation of S_8 molecules into Na_2S. These findings emphasize the synergistic effect of the Fe-Co DAC in enhancing both the adsorption and electrocatalysis of polysulfides. This synergy markedly boosts catalytic performance, representing a critical step toward the practical application of SSBs. The advantages of Fe incorporation in accelerating the catalytic process for the conversion of S_8 to Na_2S are illustrated in **Figure 6e**. Compared to Co/NC, Fe-Co/NC demonstrates enhanced sodium-ion migration, multiple adsorption sites, and rapid conversion capabilities for sodium polysulfides.

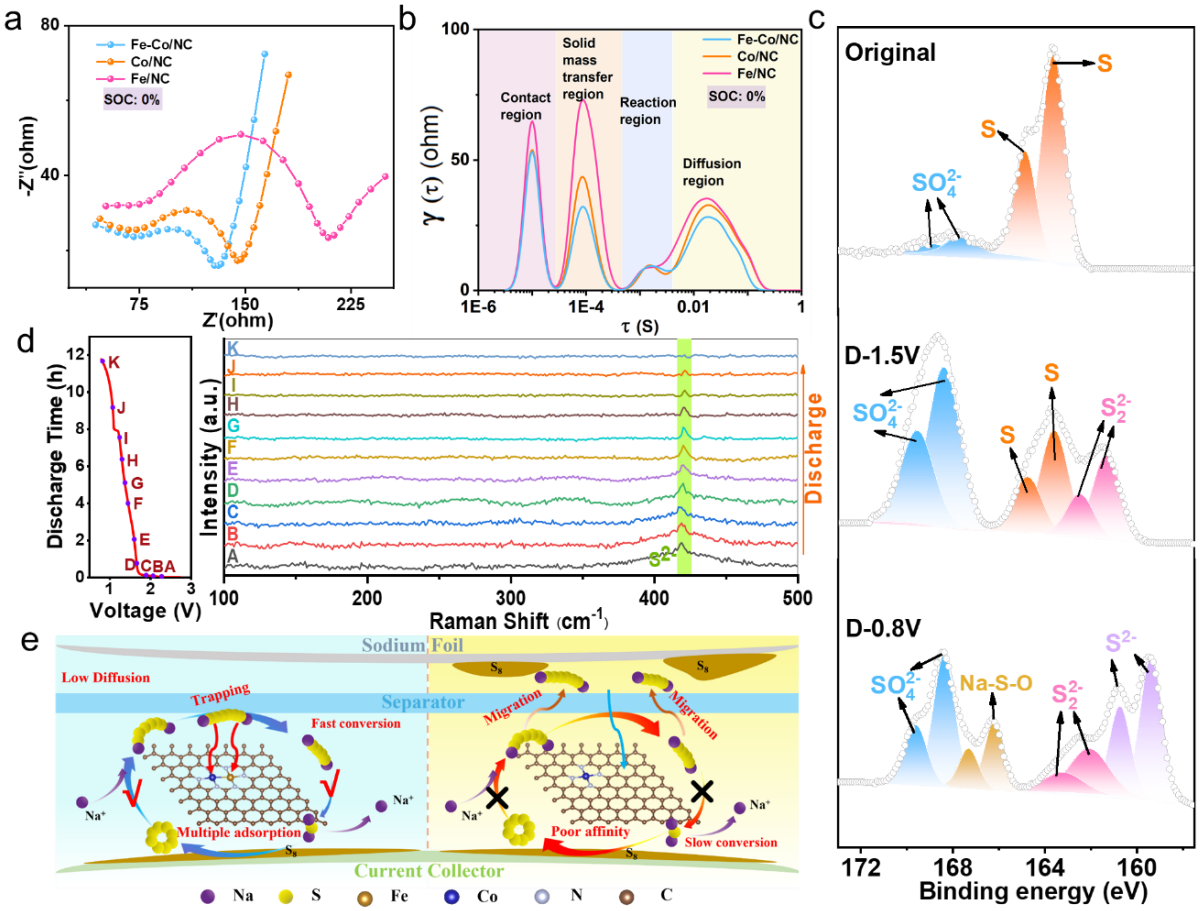

Figure 6. (a) EIS spectra of the Na–S cell with S@Fe-Co/NC, S@Co/NC and S@Fe/NC cathodes after cycling. (b) DRT profiles corresponding to impedance data of the S@Fe-Co/NC, S@Co/NC and S@Fe/NC cathode at 0% state of charge (SOC). (c) S 2p XPS spectra of the Co-Fe/NC electrode at different voltage stages (original state→discharge to 1.5V→discharge to 0.8V). (d) *In situ* time-resolved Raman spectra obtained during the discharging processes and selected Raman spectroscopy of Na-S cells based on Fe-Co/NC cathodes. (e) Schematic illustrations of the multi-site coordination mechanism of NaPSs on the matrix of Fe-Co/NC (left) and Co/NC (right).

3. Conclusions

In summary, we have successfully synthesized a Fe-Co DAC supported on N-doped hollow carbon nanospheres (Fe-Co/NC) that effectively promotes sulfur redox reaction kinetics. Comprehensive electrochemical measurements, in situ/ex situ spectroscopy analyses, and theoretical calculations reveal that the introduction of Fe single atoms around Co atoms fine-tunes the electronic distribution and adjusts the d-orbital energy levels of Co atoms. This

modification generates additional unpaired Co 3d orbital electrons, enabling more Co 3d electrons to interact with the antibonding orbitals of sulfur atoms in sulfur intermediates. This interaction regulates the adsorption-desorption equilibrium between sulfur-containing intermediates and Fe-Co/NC, thereby enhancing sulfur redox reaction activity and enabling promising battery performance in Fe-Co/NC-based SSBs. Overall, this study provides an in-depth understanding of the synergy between multi-center catalytic active sites through spin descriptors and expands the potential applications of atomically dispersed catalytic materials in SSBs.

Supporting Information

Supporting Information is available from the author.

Acknowledgements

C. H. Li thanks the China Scholarship Council for the scholarship support. D.W. Yang thanks the China Scholarship Council for the scholarship support and the funding from the National Natural Science Foundation of China (NSFC, Grant No. 22305064). J.S Li is grateful for the project supported by the Natural Science Foundation of Sichuan (2025NSFSC0139). A. Cabot acknowledges support from the 2BoSS project of the ERA-MIN3 program with the Spanish grant number PCI2022-132985/AEI/10.13039/501100011033, Generalitat de Catalunya 2021SGR01581 and European Union Next Generation EU/PRTR. ICN2 acknowledges funding from Generalitat de Catalunya 2021SGR00457. This study is part of the Advanced Materials programme and was supported by MCIN with funding from the European Union NextGenerationEU (PRTR-C17.I1) and by Generalitat de Catalunya. ICN2 is supported by the Severo Ochoa program from Spanish MCIN / AEI (Grant No.: CEX2021-001214-S) and is funded by the CERCA Programme / Generalitat de Catalunya. Part of the present work has been performed in the framework of the Universitat Autònoma de Barcelona Materials Science PhD program.

References

1. Xu, X.; Zhou, D.; Qin, X.; Lin, K.; Kang, F.; Li, B.; Shanmukaraj, D.; Rojo, T.; Armand, M.; Wang, G., A room-temperature sodium-sulfur battery with high capacity and stable cycling performance. *Nat Commun* **2018,** *9* (1), 3870.
2. Li, Z.; Wang, C.; Ling, F.; Wang, L.; Bai, R.; Shao, Y.; Chen, Q.; Yuan, H.; Yu, Y.; Tan, Y., Room-Temperature Sodium-Sulfur Batteries: Rules for Catalyst Selection and Electrode Design. *Adv Mater* **2022,** *34* (32), e2204214.
3. Yan, Z.; Zhao, L.; Wang, Y.; Zhu, Z.; Chou, S. L., The Future for Room‐Temperature Sodium–Sulfur Batteries: From Persisting Issues to Promising Solutions and Practical Applications. *Advanced Functional Materials* **2022,** *32* (36).
4. Zhang, B. W.; Sheng, T.; Wang, Y. X.; Chou, S.; Davey, K.; Dou, S. X.; Qiao, S. Z., Long‐Life Room‐Temperature Sodium–Sulfur Batteries by Virtue of Transition‐Metal‐Nanocluster–Sulfur Interactions. *Angewandte Chemie International Edition* **2019,** *58* (5), 1484-1488.
5. Ye, C.; Jiao, Y.; Chao, D.; Ling, T.; Shan, J.; Zhang, B.; Gu, Q.; Davey, K.; Wang, H.; Qiao, S. Z., Electron‐State Confinement of Polysulfides for Highly Stable Sodium–Sulfur Batteries. *Advanced Materials* **2020,** *32* (12).
6. Du, W.; Shen, K.; Qi, Y.; Gao, W.; Tao, M.; Du, G.; Bao, S. J.; Chen, M.; Chen, Y.; Xu, M., Efficient Catalytic Conversion of Polysulfides by Biomimetic Design of "Branch-Leaf" Electrode for High-Energy Sodium-Sulfur Batteries. *Nanomicro Lett* **2021,** *13* (1), 50.
7. Zhou, R.; Ren, Y.; Li, W.; Guo, M.; Wang, Y.; Chang, H.; Zhao, X.; Hu, W.; Zhou, G.; Gu, S., Rare Earth Single-Atom Catalysis for High-Performance Li-S Full Battery with Ultrahigh Capacity. *Angew Chem Int Ed Engl* **2024,** *63* (31), e202405417.
8. Liu, G.; Wang, W.; Zeng, P.; Yuan, C.; Wang, L.; Li, H.; Zhang, H.; Sun, X.; Dai, K.; Mao, J.; Li, X.; Zhang, L., Strengthened d-p Orbital Hybridization through Asymmetric Coordination Engineering of Single-Atom Catalysts for Durable Lithium-Sulfur Batteries. *Nano Lett* **2022,** *22* (15), 6366-6374.
9. Zhang, Y.; Kang, C.; Zhao, W.; Song, Y.; Zhu, J.; Huo, H.; Ma, Y.; Du, C.; Zuo, P.; Lou, S.; Yin, G., d-p Hybridization-Induced "Trapping-Coupling-Conversion" Enables High-Efficiency Nb Single-Atom Catalysis for Li-S Batteries. *J Am Chem Soc* **2023,** *145* (3), 1728-1739.
10. Han, Z.; Zhao, S.; Xiao, J.; Zhong, X.; Sheng, J.; Lv, W.; Zhang, Q.; Zhou, G.; Cheng, H. M., Engineering d-p Orbital Hybridization in Single-Atom Metal-Embedded Three-Dimensional Electrodes for Li-S Batteries. *Adv Mater* **2021,** *33* (44), e2105947.
11. Lao, Z.; Han, Z.; Ma, J.; Zhang, M.; Wu, X.; Jia, Y.; Gao, R.; Zhu, Y.; Xiao, X.; Yu, K.; Zhou, G., Band Structure Engineering and Orbital Orientation Control Constructing Dual Active Sites for Efficient Sulfur Redox Reaction. *Adv Mater* **2024,** *36* (2), e2309024.
12. Sun, T.; Huang, F.; Liu, J.; Yu, H.; Feng, X.; Feng, X.; Yang, Y.; Shu, H.; Zhang, F., Strengthened d‐p Orbital‐Hybridization of Single Atoms with Sulfur Species Induced Bidirectional Catalysis for Lithium–Sulfur Batteries. *Advanced Functional Materials* **2023,** *33* (51).
13. Li, J.; Ma, Y.; Yu, J.; Li, L.; Yang, H.; Gu, W.; Shi, J.; Wang, J.; Zhu, Y., Enhanced Methanol Electrooxidation and Supercapacitive Performance via Compositional Engineering of Colloidal Ni-Co Alloying Nanoparticles. *ChemSusChem* **2024**, e202401098.

14. Li, C.; Yu, J.; Zhang, C.; Yang, D.; Wang, J.; Li, H.; Huang, C.; Xiao, K.; Cheng, Y.; Ren, Y.; Qi, X.; Yang, T.; Li, J.; Wang, J.; Henkelman, G.; Arbiol, J.; Nan, J.; Cabot, A., Tungsten phosphide on nitrogen and phosphorus-doped carbon as a functional membrane coating enabling robust lithium-sulfur batteries. *Journal of Colloid and Interface Science* **2024,** *670*, 61-72.
15. Yang, D.; Han, Y.; Li, M.; Li, C.; Bi, W.; Gong, Q.; Zhang, J.; Zhang, J.; Zhou, Y.; Gao, H.; Arbiol, J.; Shi, Z.; Zhou, G.; Cabot, A., Highly Conductive Quasi‐1D Hexagonal Chalcogenide Perovskite Sr8Ti7S21 with Efficient Polysulfide Regulation in Lithium‐Sulfur Batteries. *Advanced Functional Materials* **2024**.
16. Jiang, Y.; Yu, Z.; Zhou, X.; Cheng, X.; Huang, H.; Liu, F.; Yang, Y.; He, S.; Pan, H.; Yang, H.; Yao, Y.; Rui, X.; Yu, Y., Single‐Atom Vanadium Catalyst Boosting Reaction Kinetics of Polysulfides in Na–S Batteries. *Advanced Materials* **2022,** *35* (8).
17. Zhang, E.; Hu, X.; Meng, L.; Qiu, M.; Chen, J.; Liu, Y.; Liu, G.; Zhuang, Z.; Zheng, X.; Zheng, L.; Wang, Y.; Tang, W.; Lu, Z.; Zhang, J.; Wen, Z.; Wang, D.; Li, Y., Single-Atom Yttrium Engineering Janus Electrode for Rechargeable Na–S Batteries. *Journal of the American Chemical Society* **2022,** *144* (41), 18995-19007.
18. Lei, Y.; Wu, C.; Lu, X.; Hua, W.; Li, S.; Liang, Y.; Liu, H.; Lai, W. H.; Gu, Q.; Cai, X.; Wang, N.; Wang, Y. X.; Chou, S. L.; Liu, H. K.; Wang, G.; Dou, S. X., Streamline Sulfur Redox Reactions to Achieve Efficient Room‐Temperature Sodium–Sulfur Batteries. *Angewandte Chemie International Edition* **2022,** *61* (16).
19. Yang, D.; Li, C.; Sharma, M.; Li, M.; Wang, J.; Wei, J.; Liu, K.; Zhang, Y.; Li, J.; Henkelman, G.; Zhang, Q.; Cabot, A., Three birds with one arrow: Multifunctional single-atom catalysts enable efficient lithium-sulfur batteries. *Energy Storage Materials* **2024,** *66*.
20. Yi, J. d.; Gao, X.; Zhou, H.; Chen, W.; Wu, Y., Design of Co‐Cu Diatomic Site Catalysts for High‐efficiency Synergistic CO2 Electroreduction at Industrial‐level Current Density. *Angewandte Chemie International Edition* **2022,** *61* (47).
21. Zhang, S.; Wu, J.; Zheng, M.; Jin, X.; Shen, Z.; Li, Z.; Wang, Y.; Wang, Q.; Wang, X.; Wei, H.; Zhang, J.; Wang, P.; Zhang, S.; Yu, L.; Dong, L.; Zhu, Q.; Zhang, H.; Lu, J., Fe/Cu diatomic catalysts for electrochemical nitrate reduction to ammonia. *Nature Communications* **2023,** *14* (1).
22. Huang, H.; Sun, M.; Li, S.; Zhang, S.; Lee, Y.; Li, Z.; Fang, J.; Chen, C.; Zhang, Y. X.; Wu, Y.; Che, Y.; Qian, S.; Zhu, W.; Tang, C.; Zhuang, Z.; Zhang, L.; Niu, Z., Enhancing H(2)O(2) Electrosynthesis at Industrial-Relevant Current in Acidic Media on Diatomic Cobalt Sites. *J Am Chem Soc* **2024,** *146* (13), 9434-9443.
23. Zhang, X.; Liu, X.; Huang, Z.-F.; Gan, L.; Zhang, S.; Jia, R.; Ajmal, M.; Pan, L.; Shi, C.; Zhang, X.; Yang, G.; Zou, J.-J., Regulating intermediate adsorption and H2O dissociation on a diatomic catalyst to promote electrocatalytic nitrate reduction to ammonia. *Energy & Environmental Science* **2024,** *17* (18), 6717-6727.
24. Zhang, B. W.; Cao, L.; Tang, C.; Tan, C.; Cheng, N.; Lai, W. H.; Wang, Y. X.; Cheng, Z. X.; Dong, J.; Kong, Y.; Dou, S. X.; Zhao, S., Atomically Dispersed Dual-Site Cathode with a Record High Sulfur Mass Loading for High-Performance Room-Temperature Sodium-Sulfur Batteries. *Adv Mater* **2023,** *35* (1), e2206828.
25. Dong, C.; Zhou, C.; Wu, M.; Yu, Y.; Yu, K.; Yan, K.; Shen, C.; Gu, J.; Yan, M.; Sun, C.; Mai, L.; Xu, X., Boosting Bi‐Directional Redox of Sulfur with Dual Metal Single Atom Pairs

in Carbon Spheres Toward High‐Rate and Long‐Cycling Lithium–Sulfur Battery. *Advanced Energy Materials* **2023,** *13* (30).
26. Sun, X.; Qiu, Y.; Jiang, B.; Chen, Z.; Zhao, C.; Zhou, H.; Yang, L.; Fan, L.; Zhang, Y.; Zhang, N., Isolated Fe-Co heteronuclear diatomic sites as efficient bifunctional catalysts for high-performance lithium-sulfur batteries. *Nat Commun* **2023,** *14* (1), 291.
27. Yang, D.; Wang, J.; Lou, C.; Li, M.; Zhang, C.; Ramon, A.; Li, C.; Tang, M.; Henkelman, G.; Xu, M.; Li, J.; Llorca, J.; Arbiol, J.; Mitlin, D.; Zhou, G.; Cabot, A., Single-Atom Catalysts with Unsaturated Co–N2 Active Sites Based on a C2N 2D-Organic Framework for Efficient Sulfur Redox Reaction. *ACS Energy Letters* **2024,** *9* (5), 2083-2091.
28. Cui, T.; Wang, Y. P.; Ye, T.; Wu, J.; Chen, Z.; Li, J.; Lei, Y.; Wang, D.; Li, Y., Engineering Dual Single-Atom Sites on 2D Ultrathin N-doped Carbon Nanosheets Attaining Ultra-Low-Temperature Zinc-Air Battery. *Angew Chem Int Ed Engl* **2022,** *61* (12), e202115219.
29. Wang, J.; Liu, W.; Luo, G.; Li, Z.; Zhao, C.; Zhang, H.; Zhu, M.; Xu, Q.; Wang, X.; Zhao, C.; Qu, Y.; Yang, Z.; Yao, T.; Li, Y.; Lin, Y.; Wu, Y.; Li, Y., Synergistic effect of well-defined dual sites boosting the oxygen reduction reaction. *Energy & Environmental Science* **2018,** *11* (12), 3375-3379.
30. Zhang, B.-W.; Sheng, T.; Liu, Y.-D.; Wang, Y.-X.; Zhang, L.; Lai, W.-H.; Wang, L.; Yang, J.; Gu, Q.-F.; Chou, S.-L.; Liu, H.-K.; Dou, S.-X., Atomic cobalt as an efficient electrocatalyst in sulfur cathodes for superior room-temperature sodium-sulfur batteries. *Nature Communications* **2018,** *9* (1).
31. Zhou, J.; Liu, X.; Zhu, L.; Zhou, J.; Guan, Y.; Chen, L.; Niu, S.; Cai, J.; Sun, D.; Zhu, Y.; Du, J.; Wang, G.; Qian, Y., Deciphering the Modulation Essence of p Bands in Co-Based Compounds on Li-S Chemistry. *Joule* **2018,** *2* (12), 2681-2693.
32. Li, C.; Yang, D.; Yu, J.; Wang, J.; Zhang, C.; Yang, T.; Huang, C.; Nan, B.; Li, J.; Arbiol, J.; Zhou, Y.; Zhang, Q.; Cabot, A., Three Birds with One Stone: Multifunctional Separators Based on SnSe Nanosheets Enable High‐Performance Li‐, Na‐ and K‐Sulfur Batteries. *Advanced Energy Materials* **2024,** *14*, 2303551.
33. Ma, C.; Wang, X.; Lan, J.; Zhang, J.; Song, K.; Chen, J.; Ge, J.; Chen, W., Dynamic Multistage Coupling of FeS2/S Enables Ultrahigh Reversible Na–S Batteries. *Advanced Functional Materials* **2022,** *33* (5).
34. Jiang, Y.; Yu, Z.; Zhou, X.; Cheng, X.; Huang, H.; Liu, F.; Yang, Y.; He, S.; Pan, H.; Yang, H.; Yao, Y.; Rui, X.; Yu, Y., Single-Atom Vanadium Catalyst Boosting Reaction Kinetics of Polysulfides in Na-S Batteries. *Adv Mater* **2023,** *35* (8), e2208873.
35. Zheng, J.; Zhang, Z., Direct Observation of the Evolutionary Process in Room-Temperature Sodium-Sulfur/Selenium Batteries Using operando Light Microscopy. *Nano Lett* **2023,** *23* (14), 6553-6559.

Abstract Graphics